Spin-affected reflexive and stretching separation of off-center droplet collision

Chengming He (何成明) ⬤,[1] Lianjie Yue (岳连捷),[1,2] and Peng Zhang (张鹏) ⬤[3,*]

[1]*Wide Range Flight Engineering Science and Application Center, Institute of Mechanics, Chinese Academy of Sciences, No. 15 Beisihuanxi Road, Beijing 100190 China*
[2]*State Key Laboratory of High Temperature Gas Dynamics, Institute of Mechanics, Chinese Academy of Sciences, No. 15 Beisihuanxi Road, Beijing 100190 China*
[3]*Department of Mechanical Engineering, The Hong Kong Polytechnic University, Hung Hom, Kowloon 999077, Hong Kong*

Recent studies have demonstrated the significant roles of droplet self-spin motion in affecting the head-on collision of binary droplets. In this paper, we present a computational study by using the volume-of-fluid method to investigate the spin-affected droplet separation of off-center collisions, which are more probable in reality and phenomenologically richer than head-on collisions. Different separation modes are identified through a parametric study with varying spinning speed and impact parameter. A prominent finding is that increasing the droplet spinning speed tends to suppress the reflexive separation and to promote the stretching separation. Physically, the reflexive separation is suppressed because the increased rotational energy reduces the excessive reflexive kinetic energy within the droplet, which is the cause for the droplet reflexive separation. The stretching separation is promoted because the increased droplet angular momentum enhances the local stretching flow within the droplet, which tends to separate the droplet. The roles of orbital angular momentum and spin angular momentum in affecting the droplet separation are further substantiated by studying the collision between two spinning droplets with either the same or opposite chirality. In addition, a theoretical model based on conservation laws is proposed to qualitatively describe the boundaries of coalescence-separation transition influenced by droplet self-spin motion.

I. INTRODUCTION

Collision between two droplets in a gaseous environment is of relevance to many natural and industrial processes, and it has been extensively studied [1–14] and reviewed [15,16] in the literature. For the simplest situation involving two identical droplets in the atmosphere, previous experimental studies [1,3,5,10,12–14] identified and interpreted some distinct collision outcomes, such as (I) coalescence, (II) bouncing, (III) coalescence, (IV) reflexive separation, and (V) stretching separation. These outcomes are schematized by a well-known collision nomogram in the two-dimensional We-B parameter space, as shown in Fig. 1. The collision Weber number, We $= \rho_l D_l U^2 / \sigma$ (ρ_l is the density of the liquid, D_l the droplet diameter, U the relative velocity, and σ the surface tension), measures the relative importance of the droplet impact energy compared to the surface energy and is limited to be of $O(10^2)$, beyond which more complex collision outcomes emerge [9,17]. The impact parameter, $B = \chi / D_l$ (χ is the projection of the mass-center connection line in the direction perpendicular to U), measures the deviation of the trajectory of droplets from that of head-on collision,
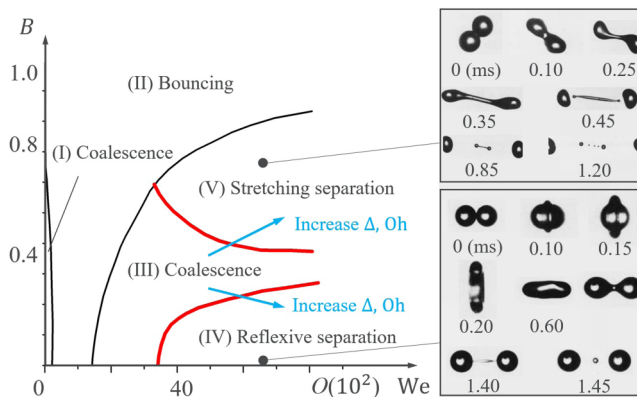
---

*pengzhang.zhang@polyu.edu.hk

FIG. 1. Schematic of droplet collision regimes in a We-B parameter space and experimental images for reflexive and stretching separation [4] for collision of identical droplets in atmosphere.

with $B = 0$ denoting head-on collision and $B = 1$ grazing collision. In this nomogram, the droplet Ohnesorge number, Oh $= \mu_l/\sqrt{\rho_l D_l \sigma}$ (where μ_l is the dynamic viscosity of the liquid), which measures the relative importance of the liquid viscous stress compared to the capillary pressure, is often not fixed but varies within a small range of values. To obtain a complete parametric description, the Ohnesorge number must be treated as an independent controlling parameter [8,12,14]. For situations more realistic than that of identical droplets in atmosphere, additional physical parameters should be considered, and a higher-dimensional parameter space may be needed for establishing a comprehensive collision nomogram. For example, the size ratio Δ measures the influence of droplet size disparity [3,10,11]; the gas-liquid density ratio (or equivalent dimensionless parameter) measures the gas pressure effect [5,18,19]; the surface tension ratio measures the Marangoni effect for collision of droplets of unlike liquids [20–23].

Among various droplet outcomes, droplet coalescence and separation are often of great interest because they may significantly change the droplet size distribution in dispersed liquid-gas flows. Given other collision parameters being fixed, two colliding droplets with a small impact kinetic energy (i.e., at small We) tend to merge into a larger droplet. Although the colliding droplets may bounce back at intermediate We, they tend to separate into two large bulks of liquid with a certain number of satellite droplets if the impact kinetic energy is substantially larger than the surface energy (i.e., at sufficiently large We) [3–5]. As Oh and Δ increase, the regime boundaries between coalescence and separation tend to move towards a larger We, because the augmented viscous dissipation of the droplet internal flow stabilizes the merged droplet [11,12,24]. The droplet separation and satellite droplet formation have been found to be important physics components in modeling various spray processes [25–27].

The regimes of coalescence and separation (including reflexive separation and stretching separation) are shown in Fig. 1. In a certain range of We, droplet collision outcomes show a nonmonotonic variation from reflexive separation to coalescence and to stretching separation as increasing B [3–6,10,11]. For collisions at small B [4,5], the reflexive separation (regime IV) occurs when the kinetic energy of droplet collision is substantially larger than the surface energy of the droplets. The droplets may still possess a significant amount of translational kinetic energy upon their coalescence. If the viscous internal flow within the coalesced droplet does not rapidly dissipate the excessive kinetic energy, the coalesced droplet cannot be held by its surface tension and will be elongated in the direction of droplet collision to result in a separation. For collisions at larger B, the colliding droplets tend to form a long ligament by the stretching-flow motion, and the stretching separation (regime V) occurs when the kinetic energy of the liquid ligament is larger than the sum of surface energy and stretching-flow-induced viscous dissipation [3,4]. Furthermore, for collisions

at intermediate B and We of $O(10^2)$ or higher, a new regime named "rotational separation" was identified [28], which was interpreted by the balance between rotational energy and surface energy [1,4].

In realistic situations droplet collision is more complicated than in the cases discussed above due to the presence of droplet self-spin motion. The previous experimental [3,4] and numerical [29–31] studies have demonstrated that two initially nonspinning droplets undergoing off-center collisions (leading to either bouncing or coalescence) can generate significant spinning motion of droplets. This is because the initial orbital angular momentum of the two droplet system [30,31] can be partially converted into the spin angular momentum of each droplet. It is very likely that every droplet in a real spray system would possess a spin motion of certain speed if droplet interaction is present in the system.

The previous understanding of droplet collision would be modulated by considering the presence of droplet spin. For the head-on bouncing between spinning droplets [32], the spinning droplet can induce significant nonaxisymmetric droplet deformation because of the conversion of the spin angular momentum into the orbital angular momentum. The interchange between orbital and spin angular momentums during the collision process is of significance because it can influence the postcollision velocities of bouncing droplets. For head-on coalescence between a spinning droplet and a nonspinning droplet of equal size [32], the spinning motion can promote the mass intermingling of droplets because the locally nonuniform mass exchange occurs at the early collision stage by nonaxisymmetric flow and is further stretched along the filament at later collision stages. Apart from the study of spinning effects on droplet bouncing and coalescence, the spin-affected droplet separation and subsequent satellite droplet formation are highly probable in practical dense sprays, but relevant studies have been rare in the literature.

In this paper, we present a computational study to investigate the spinning effects on the droplet separation. The presentation of the study is organized as follows. The numerical methodology and specifications are described in Sec. II. The separation modes and mechanisms affected by impact parameter and droplet spinning speed are presented in Sec. III, followed by the influences of chirality of droplet self-spin motion on reflexive and stretching separations in Sec. IV. Finally, a theoretical model for reflexive and stretching separation is proposed to account for the boundary transition influenced by the chirality of droplet spin motion in Sec. V.

II. COMPUTATIONAL METHODOLOGY AND SPECIFICATIONS

A. Methodology and validations

The three-dimensional (3D) continuity and incompressible Navier-Stokes equations,

$$\nabla \cdot \boldsymbol{u} = 0, \tag{1}$$

$$\rho(\partial \boldsymbol{u}/\partial t + \boldsymbol{u} \cdot \nabla \boldsymbol{u}) = -\nabla p + \nabla \cdot (2\mu \boldsymbol{D}) + \sigma \kappa \boldsymbol{n} \delta_s, \tag{2}$$

are solved by using the classic fractional-step projection method, where $\boldsymbol{u}$ is the velocity vector, ρ the density, p the pressure, μ the dynamic viscosity, and $\boldsymbol{D}$ the strain rate tensor defined as $D_{ij} = (\partial_j u_i + \partial_i u_j)/2$. In the surface tension term $\sigma \kappa \boldsymbol{n} \delta_s$, δ_s is a Dirac delta function, σ the surface tension coefficient, κ the local curvature, and the unit vector $\boldsymbol{n}$ normal to the local interface.

To solve both the gas and liquid phases, the density and viscosity are constructed by the volume fraction as $\rho = c\rho_l + (1-c)\rho_g$ and $\mu = c\mu_l + (1-c)\mu_g$, in which the subscripts l and g denote the liquid and gas phases, respectively. The volume fraction c satisfies the advection equation

$$\partial c/\partial t + \nabla \cdot (c\boldsymbol{u}) = 0, \tag{3}$$

with $c = 1$ for the liquid phase, $c = 0$ for the gas phase, and $0 < c < 1$ for the gas-liquid interface. The present study adopts the volume-of-fluid (VOF) method, which has been implemented in the

open source code, GERRIS [33,34], featuring the 3D octree adaptive mesh refinement, the geometrical VOF interface reconstruction, and continuum surface force with height function curvature estimation. GERRIS has been demonstrated to be competent for high-fidelity simulation of a wide range of multiphase flow problems [29–32,35–40].

A major challenge of VOF simulation of droplet collision lies in the absence of subgrid models describing the rarefied gas effects and the van der Waals force [41] within the gas film, thereby prohibiting the physically realistic prediction of droplet coalescence and separation. A coarse mesh would result in a "premature" coalescence of droplets without prominent droplet deformation. Thus, the successful simulation of droplet coalescence and subsequent collision dynamics in previous studies [29,35,38] was obtained by choosing an appropriate mesh resolution in the vicinity of the interface. However, it is noted that the resolution of gas film drainage is not a significant issue for the simulation of droplet separation at large We. This is because the drainage of gas film occurs at a much shorter timescale compared with that of the entire process of the coalescence and separation of droplets. In addition, the energy budget during the gas film drainage accounts for a very small portion of the total energy budget. As a result, the computational uncertainties of droplet coalescence caused by a relatively coarse mesh for gas film will not result in significant difference to the "long-time" dynamics of droplet deformation and separation. The VOF simulation of Chen *et al.* [29,42] shows that a maximum interface mesh refinement of level 11 is required to produce the physically correct droplet bouncing at We = 8.6 [29], but a mesh refinement of level 8 can produce satisfactory results of droplet separation at We = 61.4 [42]. Similarly, the level-set method [43] and lattice Boltzmann method (LBM) [21,44] have also been used to simulate droplet separation with a reasonably refined mesh and without any subgrid models for rarefied gas effects and the van der Waals force.

To justify the computational approach discussed above, the experimental validation and grid independence analysis are shown in Fig. 2 for the case at We = 61.4, B = 0.06, and Oh = 0.028 of Qian and Law [5]. To improve computational efficiency, the entire computational domain is divided into three physical zones, namely, the gas, the droplet, and the interface zones, and different mesh refinement levels (N_g, N_l, N_i) are used in these zones. The simulation results by Chen *et al.* [42] with a mesh refinement level of (4, 7, 8) are shown in Fig. 2(b) for comparison. The present results with the same mesh refinement level are shown in Fig. 2(c). The presented simulation results are those having the most agreement of droplet deformation with the experimental images, whereas the time discrepancies between them could serve as an indicator for simulation errors. It is seen that the experimental and simulation times display slight discrepancies throughout the entire collision process, and the time errors are less than 8%. A typical simulation run with the mesh refinement level (4, 7, 8) results in 3.73×10^6 grid points in the entire droplet, taking about 200 h of real time to run the simulation up to $T = 2.0$ on two Intel XeonGold-6150 processors with 72 cores (36 cores for each processor).

B. Problem description and numerical specifications

The 3D computational domain of droplet collision is illustrated from different perspectives, as shown in Fig. 3. Two droplets of diameter D are specified to collide along the x direction with a relative translational velocity U, and therefore they have zero relative velocities in the y and z directions. Without losing generality, the translational velocity components for droplet O_1 and O_2 are set as $-U/2$ and $U/2$ along the x direction, respectively, so that the linear momentum of the entire mass-center system remains zero. For off-center collisions, the deviation of the mass centers from the head-on collision is qualified by χ, which is defined as the projection of the connection line O_1O_2 (hereinafter referred to as $\overline{O_1O_2}$) along the z direction. The spin axis l_{O_1} can be specified by a polar angle θ with respect to the z axis and an azimuthal angle φ to the x axis. In our previous study [32], we deliberately fixed the polar angle $\theta = \pi/2$ and varied the azimuthal angle φ in the range of $0 < \varphi < \pi/2$, because the situations with varying θ are equivalent for the axisymmetric head-on droplet collision. As a result, the initial spin angular velocity can be expressed
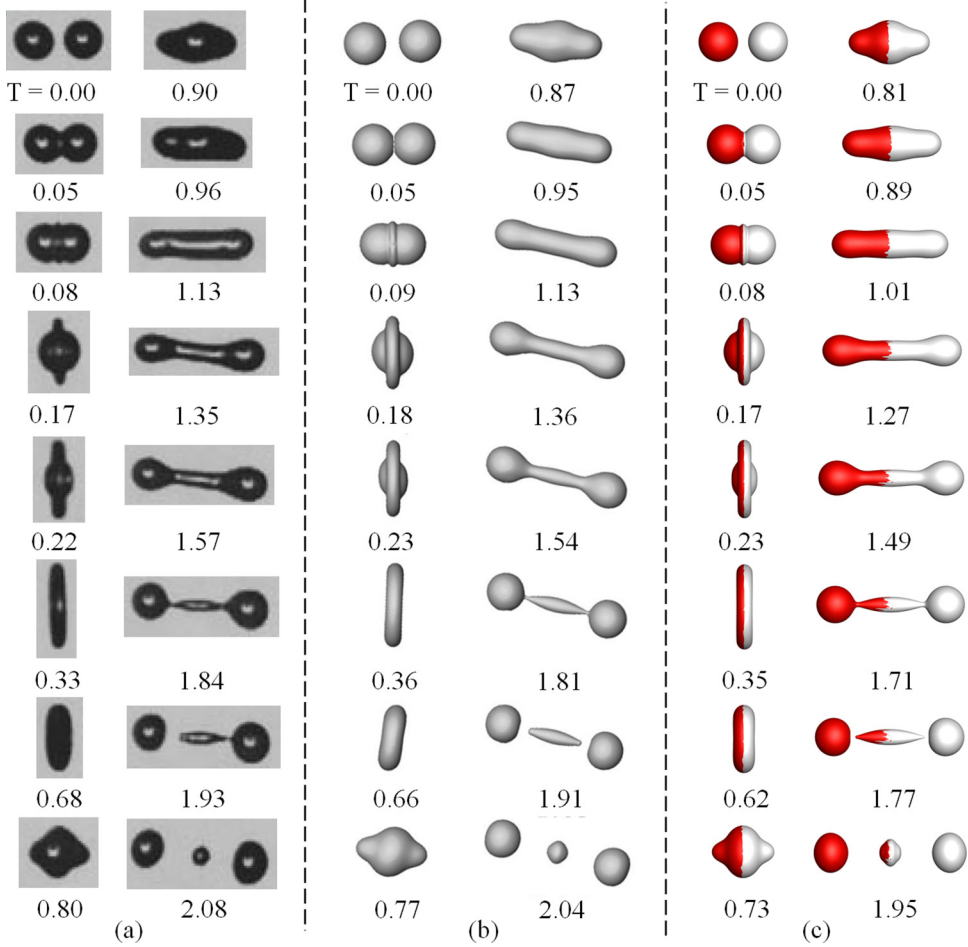
FIG. 2. Comparison of (a) experimental images from Qian and Law [5], (b) simulation results from Chen *et al.* [42], and (c) the present results, for the nearly head-on separation of identical droplets at We = 61.4, Oh = 0.028, and B = 0.06. The dimensionless time $T = t/t_{osc}$ and $t_{osc} = (\rho_l R_l^3/\sigma)^{1/2} = 1.06$ ms.

as $\boldsymbol{\omega}_0 = (-\omega_0\cos\varphi, -\omega_0\sin\varphi, 0)$, and the spinning velocity components of droplet O_1 are given by $H(\phi-1)\boldsymbol{\omega}_0 \times (\boldsymbol{r} - \boldsymbol{R}_{O_1})$, where ϕ is the color functio n with $\phi = 1$ in the spinning droplet O_1 and otherwise $\phi = 0$, and the Heaviside step function H ensures the assignment of spin to droplet O_1 only. The domain is $6D$ in length and $4D$ in both width and height; all the boundaries are specified with the free outflow boundary conditions.

To simplify the parametric study in the present work, the polar angle θ is fixed at $\pi/2$ and the azimuthal angle φ is fixed at $\pi/2$. This is because the nonaxisymmetric flow characteristics induced by the droplet spin are the most prominent at $\varphi = \pi/2$, owing to the strongest interaction between the spinning motion and the translational motion [32]. This simplification is justified by examining the simulation results shown in Fig. 4. The deformation of the head-on collision between two nonspinning droplets is axisymmetric by x axis and "mirror symmetry" with respect to the (*y-z*) plane, as seen in Fig. 4(a). For collisions between a spinning droplet and a nonspinning droplet, as shown in Figs. 4(b)–4(d) with varying φ from 0 to $\pi/2$, the droplet deformation is deviated from the head-on collision owing to the conversion of spin angular momentum into orbital angular momentum. The droplet separation followed by the asymmetric pinch-off of the ligament
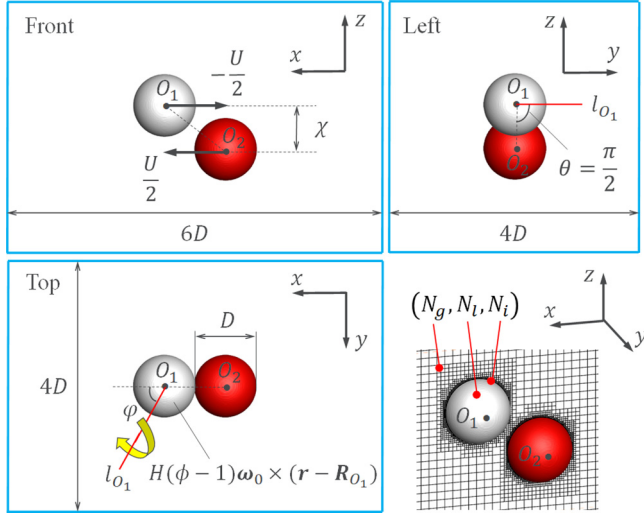
FIG. 3. Three-dimensional computational setup for an off-center collision between a spinning droplet O_1 and a nonspinning droplet O_2.
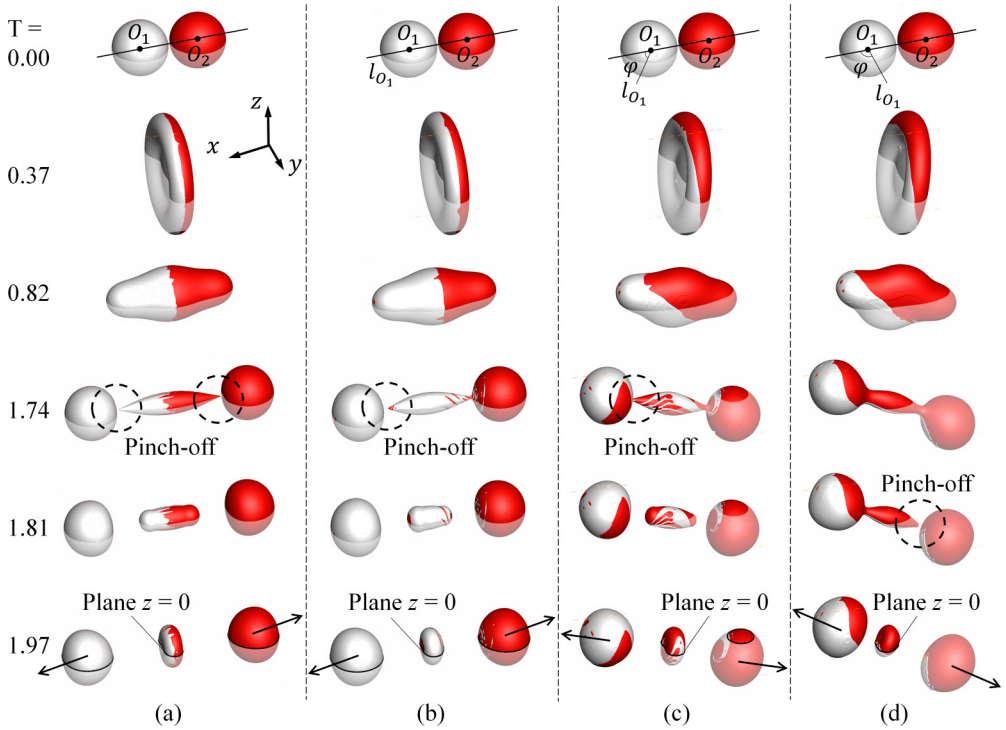

FIG. 4. Evolution of droplet deformation upon a head-on collision of (a) two nonspinning droplets and of a spinning droplet O_1 and a nonspinning droplet O_2 with varying azimuthal angle of droplet O_1 (b) $\varphi = 0$, (c) $\varphi = \pi/4$, and (d) $\varphi = \pi/2$, at We = 61.4, Oh = 0.028, and $\omega_0 = 3$.

is delayed when compared to that of nonspinning droplet collision owing to the enhanced viscous dissipation induced by the droplet's translational impacting motion and droplet spinning motion. The asymmetry from the z plane reaches its maximum at $\varphi = \pi/2$, where there is the strongest interaction between the spinning motion and the translational motion.

In real situations, the spinning speed of the droplets in a spray must have a distribution in which both very large and very small speeds are improbable. To accurately determine the distribution, we need to solve the transport equation of droplet distribution function $f(t, \boldsymbol{x}, \boldsymbol{v}, D, \boldsymbol{\omega})$, in which the additional variable $\boldsymbol{\omega}$ characterizes the droplet spinning motion. This is the central problem of spray simulation, and various computational approaches have been developed for it. In the present work, we estimated the most probable spinning speed based on the understanding that the spinning motion of droplets is often generated by the preceding droplet collisions, and that the spinning speed increases with increasing the collision Weber number. Due to the large density ratio of liquid to gas, the droplet spin caused by the ambient shear flow (e.g., turbulent eddies) is assumed to be secondary. Our previous studies [32,45] have showed that the nondimensional angular velocity ω of droplet spin nonmonotonically varies with the impact parameter and is $\omega_0 = 1.0$–3.0 for We $= 9$–20, corresponding to the dimensional angular velocity of 1000–3000 rad/s. We note that a larger ω_0 may be probable in practical sprays because droplets can bounce off at larger Weber number under the elevated pressure environment [5] of the combustion chamber. However, in our preliminary studies, we simulated a single spinning droplet with larger angular velocities, and it is seen that the droplet is not spherical or even that it cannot hold its interface intact as the spin angular velocity increases to $\omega_0 = 6$. The initially nonspherical droplet can cause the collision outcomes to be completely different. Collision of droplets with high spin angular velocities would be an interesting problem and merits future studies. Consequently, we limited our scope of investigation to the range of spin angular velocity $\omega_0 = 0$–6.

In addition, to further simplify the problem but not to lose generality, this study restricts its scope to the collision between two equal-sized droplets ($\Delta = 1.0$) so as to avoid unnecessary complexity of geometrical asymmetry and size disparity. Furthermore, we recognized that the postcollision velocity vector of the separated droplets may be affected by the spinning axis (θ and φ), and the parametric study of spinning axis orientation will be considered in our future studies. Consequently, the present numerical study focuses on the controlling parameters in the range of We $= 40$–85, $B = 0$–1.0, $\omega_0 = 0$–6, and Oh $= 0.028$.

III. EFFECTS OF DROPLET SPIN SPEED AND IMPACT PARAMETER

A. Separation modes affected by ω_0 at different B

Figure 5 shows the droplet separation affected by different droplet spinning speed ω_0 and impact parameter B. To facilitate the physical understanding from the perspective of angular momentum conversion, the consequence of varying ω_0 and B is also characterized as the change of spin angular momentum $\boldsymbol{L}_{s1}$ of droplet O_1 with respect to the spinning axis across its mass center and the orbital angular momentum $\boldsymbol{L}_o$ with respect to the y axis for two droplets system, respectively.

The time-dependent angular momentums $\boldsymbol{L}_{s1}$ and $\boldsymbol{L}_o$ are calculated by

$$\boldsymbol{L}_{s1}(t) = \int_V \rho_l H(\phi - 1)\big(\boldsymbol{r} - \boldsymbol{R}_{O_1}\big) \times \boldsymbol{v} dV', \tag{4}$$

and

$$\boldsymbol{L}_o(t) = \int_V \Big[\rho_l H(\phi - 1)\boldsymbol{R}_{O_1} + \rho_l H(c - \phi - 1)\boldsymbol{R}_{O_2} \Big] \times \boldsymbol{v} dV', \tag{5}$$

where H is the Heaviside step function, ϕ the color function used in VOF simulation, c the volume fraction, $\boldsymbol{r}$ and $\boldsymbol{v}$ the position vector and velocity vector, and V the integral volume of liquid and gas
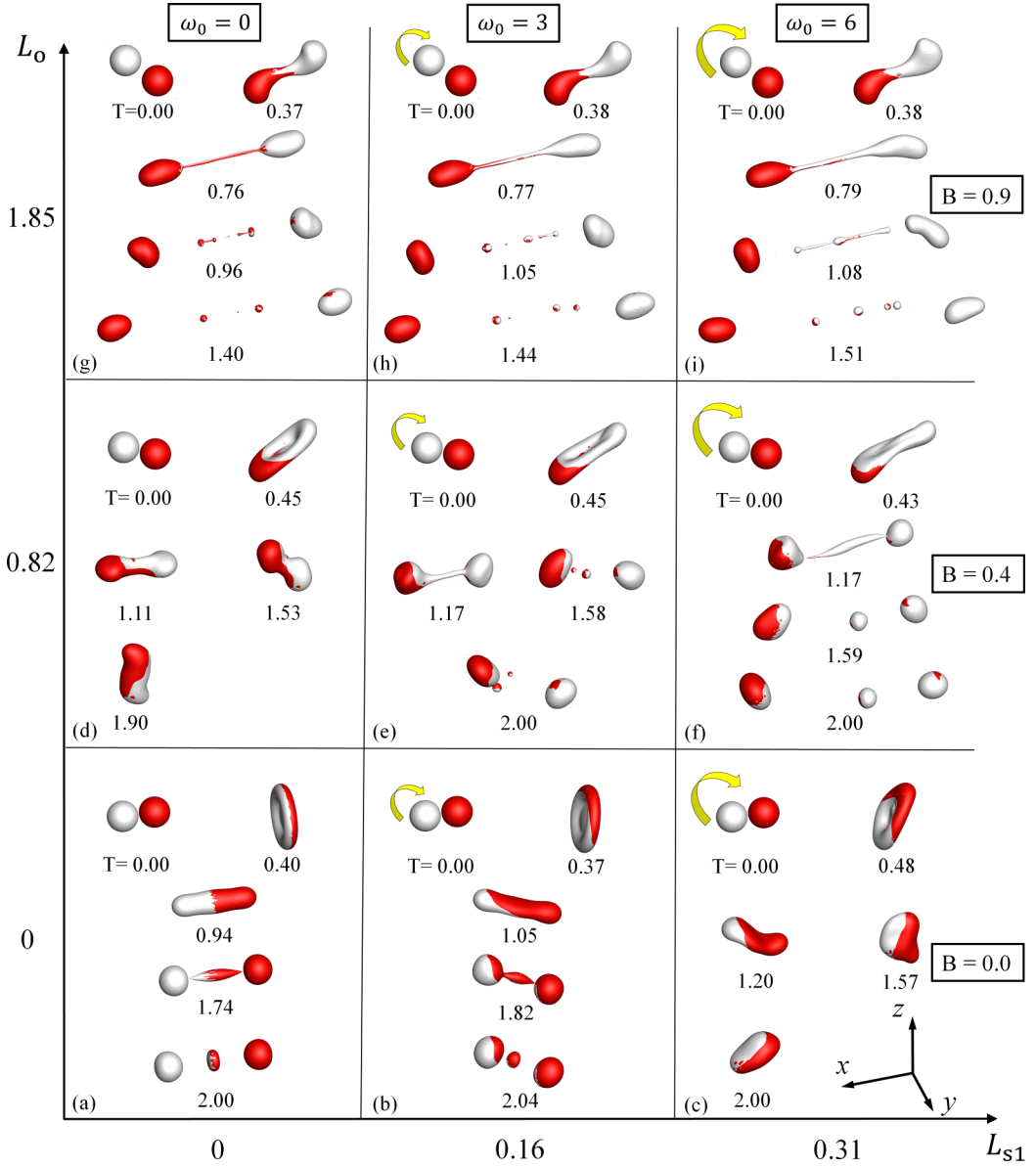
FIG. 5. Collision between a spinning droplet and a nonspinning droplet with varying spinning speed ω_0 and impact parameter B at We = 61.4 and Oh = 0.028.

phases. The time-dependent $\boldsymbol{R}_{O_1}$ and $\boldsymbol{R}_{O_2}$ are the position vectors of the mass centers O_1 and O_2 for two droplets, defined by

$$\boldsymbol{R}_{O_1}(t) = \int_V \rho_l H(\phi - 1)\boldsymbol{r}dV'/M_1, \tag{6a}$$

$$\boldsymbol{R}_{O_2}(t) = \int_V \rho_l H(c - \phi - 1)\boldsymbol{r}dV'/M_2. \tag{6b}$$

Although L_{s1} and L_o change with time during droplet collision, the conserved total angular momentum $L_t = L_o + L_{s1}$ poses an additional restriction on the motion of droplets. Furthermore, owing to the polar angle θ and azimuthal angle φ being fixed at $\pi/2$ in the present study, the angular momentums L_o and L_{s1} (and hence L_t) have a nonzero component only in the y direction. The y components, L_{s1} and L_o, at the initial time are given by

$$L_{s1}(t=0) = \frac{2}{5}\left(\frac{4}{3}\pi R^3 \rho_l\right)R^2\omega_0, \tag{7a}$$

$$L_o(t=0) = \frac{1}{2}\left(\frac{4}{3}\pi R^3 \rho_l\right)(2R)UB. \tag{7b}$$

Three cases of head-on collisions at $B = 0.0$ are shown in Figs. 5(a)–5(c), where the nonspinning case with $\omega_0 = 0$ is also shown as a benchmark case for comparison. It is seen that the benchmark case clearly shows the typical physical phenomena of reflexive separation. Specifically, the colliding droplets undergo the following stages: (I) the initial coalescence, (II) the radial deformation to form a pancake shape, (III) the retraction motion under surface tension towards the axis (the x direction), (IV) the stretching motion along the axis owing to the droplet inertia, (V) the formation of a liquid ligament being attenuated at the ends, (VI) the final pinch-off of the ligament simultaneously at the two sufficiently attenuated ends, and (VII) the contraction of the pinched-off ligament under surface tension to form a satellite droplet. For the spinning case with $\omega_0 = 3$, the colliding droplets still undergo the same stages as described above but have apparent nonaxisymmetric appearances. Particularly, the unsymmetrical liquid ligament pinches off first from the attenuated end connected to the nonspinning droplet. Such a nonaxisymmetric droplet collision becomes so significant for the case with $\omega_0 = 6$ that the droplet separation is completely suppressed.

For the collisions at intermediate $B = 0.4$, which are shown in Figs. 5(d)–5(f), the nonspinning case shows no separation but permanent coalescence; however, the stretching separation is manifested for the spinning cases. It is seen that a longer liquid ligament is formed with increasing ω_0. For the collisions at larger $B = 0.9$, as shown in Figs. 5(g)–5(i), the formed ligament is elongated with increasing ω_0, and it can break up into multiple satellite droplets of different sizes.

B. Separation mechanisms affected by ω_0

For the collisions at small B, the reflexive separation is suppressed by increasing ω_0. This observation can be explained as the enhanced viscous dissipation [32] induced by the interaction between the spinning and translational motions of droplets. Specifically, the viscous dissipation rate (VDR) [30] is calculated by

$$\text{VDR} = \frac{\mu_l}{2}(\partial_j u_i + \partial_i u_j)^2 = 2\mu_l D_{ij}^2, \tag{8}$$

and is shown in Fig. 6. It is clearly seen that the viscous dissipation is enhanced around the outward deformation interface, which also has large rotational velocity induced by the droplet spin. In addition, the tendency of reflexive flow accounting for the reflexive separation is reduced by the enhanced inner rotating flow. If the kinetic energy of the droplet reflexive motion is not sufficiently large to overcome the surface tension energy, it will eventually be dissipated during the droplet oscillation process, consequently leading to droplet coalescence.

It has been shown in Figs. 5(d)–5(f) that the stretching separation is promoted with increasing ω_0 for the collisions at intermediate $B = 0.4$. This is because the total angular momentum ($L_t = L_o + L_{s1}$) of the merged droplet is increased so as to enhance droplet stretching and hence droplet separation. Specifically, the vorticity ω_y and streamlines in the y direction are shown in Fig. 7, and they can reflect the local spinning motion during droplet deformation. It is seen that the vorticity distribution shows a point symmetry with respect to the origin for the nonspinning case, whereas the point symmetry is broken due to the nonzero initial vorticity of the spinning droplet. The liquid mass from the spinning droplet has a larger kinetic energy (KE) than that from the initially nonspinning
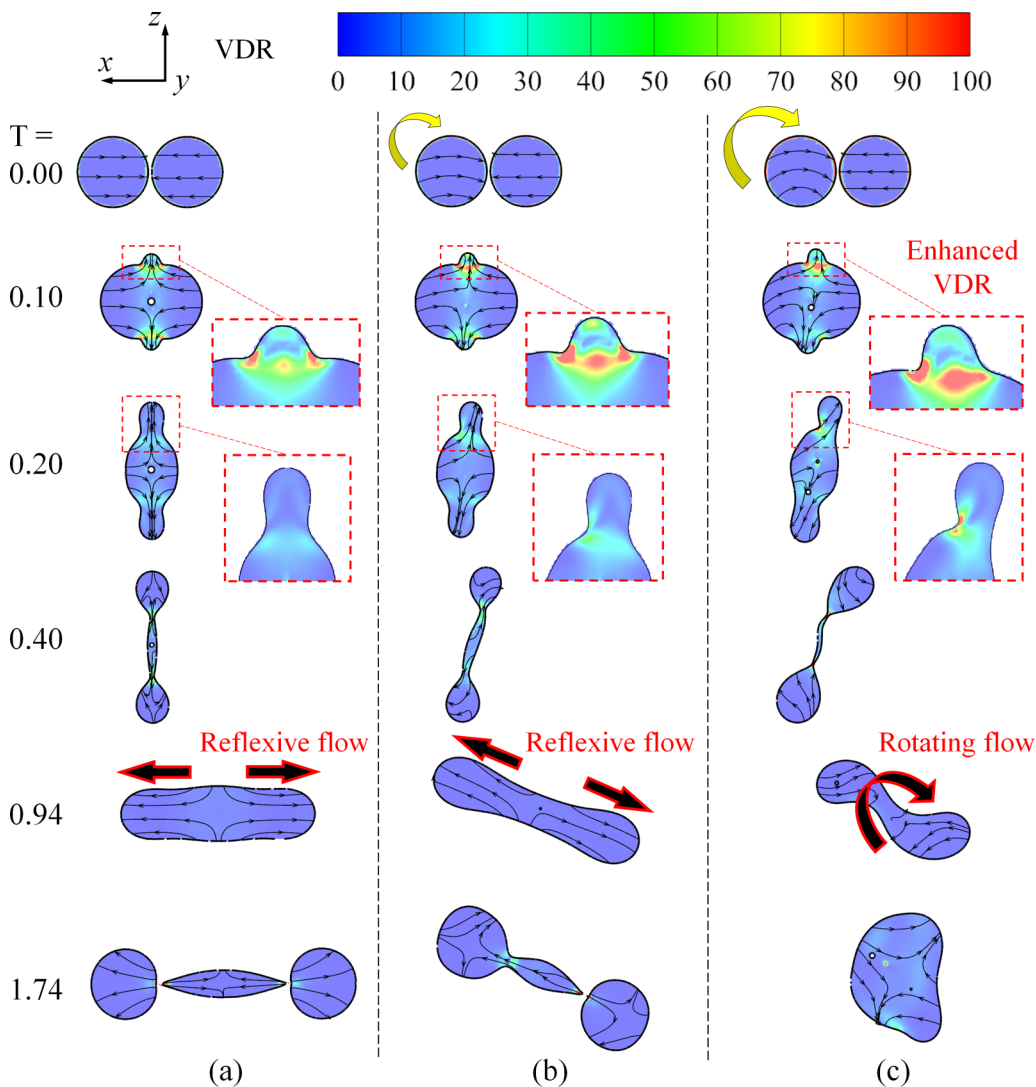
FIG. 6. Contour of the viscous dissipation rate (VDR) and streamlines for the three cases of reflexive separation at $B = 0.0$ that are shown in Figs. 5(a)–5(c) with (a) $\omega_0 = 0$, (b) $\omega_0 = 3$, and (c) $\omega_0 = 6$.

droplet, as shown by the embedded contour of KE at $T = 0.22$. The locally enhanced KE on one side of the merged droplet tends to elongate the merged droplet to form a longer ligament, as shown in Fig. 7(c). The enhanced local stretching flow owing to the droplet spin can overcome the surface tension to separate the ligament.

For the collisions at $B = 0.9$ that are shown in Figs. 5(g)–5(i), the spinning motion can lead to a longer ligament and then break up into more satellite droplets with increasing ω_0. This can be explained by the same mechanism of the stretching separation at intermediate B as the stretching effect is enhanced by the droplet self-spin. It is interesting to see in Fig. 8 that the liquid mass from the initial spinning droplet can have a residual spin angular momentum. The vorticity of the residual spin is enhanced with increasing ω_0.
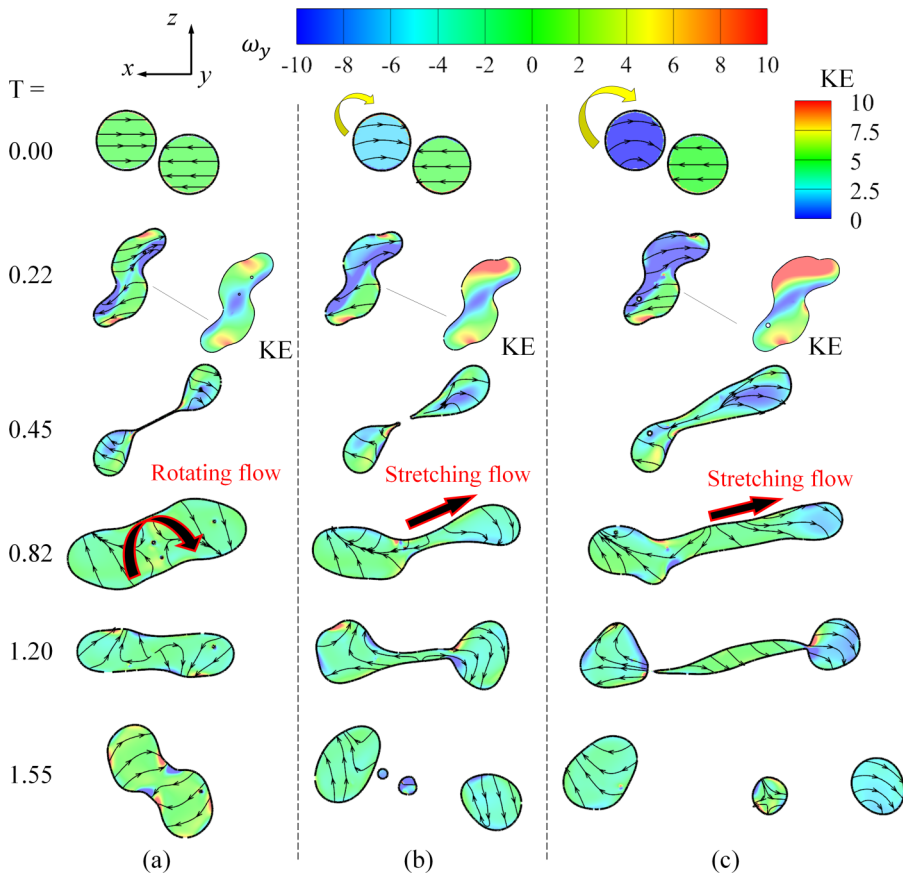
FIG. 7. Contour of the vorticity and kinetic energy (KE) fields and streamlines for the three cases of stretching separation at $B = 0.4$ that are shown in Figs. 5(d)–5(f) with (a) $\omega_0 = 0$, (b) $\omega_0 = 3$, and (c) $\omega_0 = 6$.

IV. EFFECTS OF DROPLET SPIN AND ITS CHIRALITY

A. Influences of droplet spin chirality on We-B regime nomogram

It is noted that the spinning motion of the droplet is set up so that its angular momentum has the same direction as the orbital angular momentum. Consequently, their synergetic influence on the droplet collision is through the scalar total angular momentum $(L_o + L_{s1})$. It is a natural question to ask what influence the droplet spinning direction has; it apparently can change the total angular momentum L_t and hence the rotational energy of the collision system. Considering the angle $(0 \leqslant \psi \leqslant \pi)$ between the spin and the orbital angular momentum, we can infer that the influence should be minimal at $\psi = \pi/2$ (orthogonality) and be maximal at either $\psi = 0$ (corresponding to the cases discussed so far) or $\psi = \pi$, which will be discussed as follows.

One of the most prominent effects of the spin chirality is its effect on the stretching separation, as shown in the regime nomogram in Fig. 9. Compared with the nonspinning cases, as shown in Fig. 9(a), the stretching separation-coalescence regime boundary moves down to smaller B in Fig. 9(b) for the "positive" spin, which results in the addition of the orbital and spin angular momentums $(L_o + L_{s1})$, and the regime boundary moves up to larger B in Fig. 9(c) for the "negative" spin, which results in the counteraction of the angular momentums $(L_o - L_{s1})$. This finding is consistent with the above discussions for Fig. 7, that a larger value of L_t could generate a more significant local stretching flow and therefore a longer liquid ligament leading to a stretching
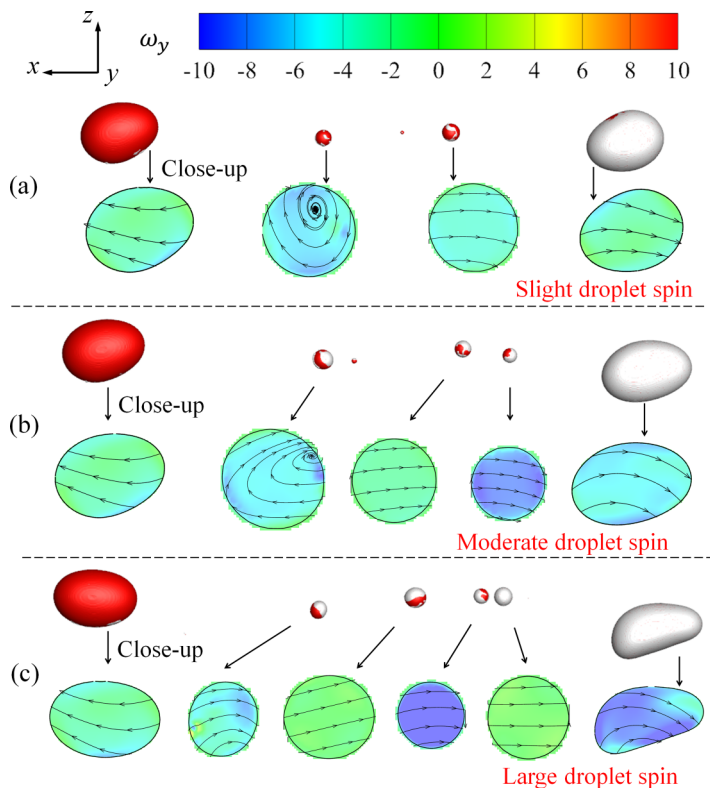
FIG. 8. Contour of the vorticity field and satellite droplet formation upon the three cases of nearly grazing collision at $B = 0.9$ that are shown in Figs. 5(g)–5(i) with (a) $\omega_0 = 0$, (b) $\omega_0 = 3$, and (c) $\omega_0 = 6$.

separation even if at a smaller B. Similarly, a smaller L_t reduces the local stretching inertia, and a larger B is therefore necessary for stretching separation of the merged droplet.

Another prominent effect of the spin chirality is that on the reflexive separation. Specifically, the reflexive separation is suppressed by the positive spin as seen in Fig. 9(b), whereas it is negligibly influenced by the negative spin as seen in Fig. 9(c). This can be explained from a perspective of energy budget by using a representative case of the nearly head-on collision at We = 61.4 and $B = 0.15$, as shown in Fig. 10. As discussed in the preceding section, the reflexive separation is influenced by the competition between the viscous dissipation within the reflexive flow and the rotating flow that diminishes the reflexive flow. Although the total energy (TE) for three cases is approximately the same, the kinetic energy (KE) and surface energy (SE) for the case (b) with $L_t = L_o + L_{s1}$ are different from the others because the reflexive separation does not happen for this case. It is also noted that there are minor differences of the total viscous dissipation rate, TVDR(T) $= \int_V$ VDR $H(c-1)dV$, and the time accumulated viscous dissipation energy, TVDE $= \int_0^T$ TVDR$(T)dT$ [30] for the three cases. It is inferred that the viscous dissipation is not a decisive factor accounting for the influence of the spin chirality on the reflexive separation.

The vorticity field that reflects the local inner flow is illustrated in Fig. 11. Compared with the reflexive separation in cases (a) and (c), the droplet spin in case (b) leads to a nonuniform vorticity distribution on the round head of the ligament. The vorticity diffusion due to the vorticity nonuniformity would induce a net rotating flow from the head of the ligament to its center and therefore strengthen the ligament against being separated. For case (c), the slightly nonuniform vorticity distribution is insufficient to induce a prominent rotating flow to counteract the reflexive flow so that the reflexive separation occurs.
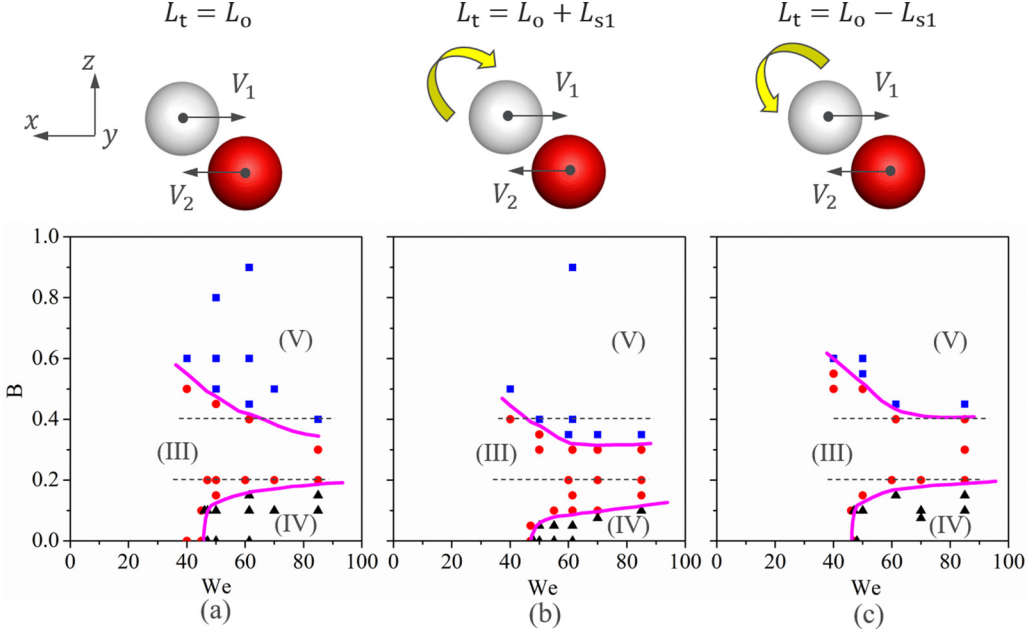
FIG. 9. Influence of chirality of droplet spin on the transition of coalescence-separation boundary at $Oh = 0.028$ for the case of (a) two nonspinning droplets and the cases of one spinning droplet with (b) $\boldsymbol{\omega}_0\hat{y} = -3$ and (c) $\boldsymbol{\omega}_0\hat{y} = 3$.

B. Separation of two spinning droplets with different chirality

For a complete discussion about the chirality effects, the collisions between two spinning droplets with either opposite or the same spinning directions are examined, based on two representative cases of $B = 0.0$ and $B = 0.4$ from Fig. 5 (at $We = 61.4$, $Oh = 0.028$, and $\omega_0 = 3$).

For the head-on collision between two spinning droplets with opposite chirality in Fig. 12(a), the droplet deformation and vorticity contour are of a mirror symmetry with respect to the interaction (y-z) plane because of $L_t = 0$. The reflexive separation is observed, although a shorter ligament and a smaller satellite droplet appear when compared with the case shown in Fig. 4(d) for a spinning droplet and a nonspinning droplet. For collision droplets with same chirality in Fig. 12(b), the reflexive separation is suppressed because both the rotating flow and rotational kinetic energy are enhanced by the increase of angular momentum $L_t = 2L_{s1}$. It consolidates our understanding that the rotational kinetic energy associated with the angular momentum can suppress the reflexive separation for the nearly head-on collision.

For the off-center collision between two spinning droplets shown in Fig. 13, the situation is more complex than that of the head-on collision in Fig. 12 due to the nonzero L_o. Thus, we compare two different situations with the reference spin of droplet O_1 being clockwise (positive) or anticlockwise (negative) that can increase or decrease total angular momentum, respectively. In addition, to characterizing the roles of initial local stretching flow on separation for each droplet, the value of orbital angular momentum L_o has been manually divided into two identical components of L_{o1} and L_{o2} for each droplet to facilitate the discussion.

By comparing the opposite droplet spin direction in Fig. 13(a) and the collision between two nonspinning droplets in Fig. 5(d), they have the same $L_t = L_o$; however, the stretching separation is observed in Fig. 13(a). This is because the initial total angular momentum for droplet O_1 is $L_{o1} + L_{s1}$, which leads to an enhanced local stretching flow and promotes a long ligament formation and thereby stretching separation. Conversely, $L_{o2} - L_{s2}$ for droplet O_2 causes a reduced local stretching
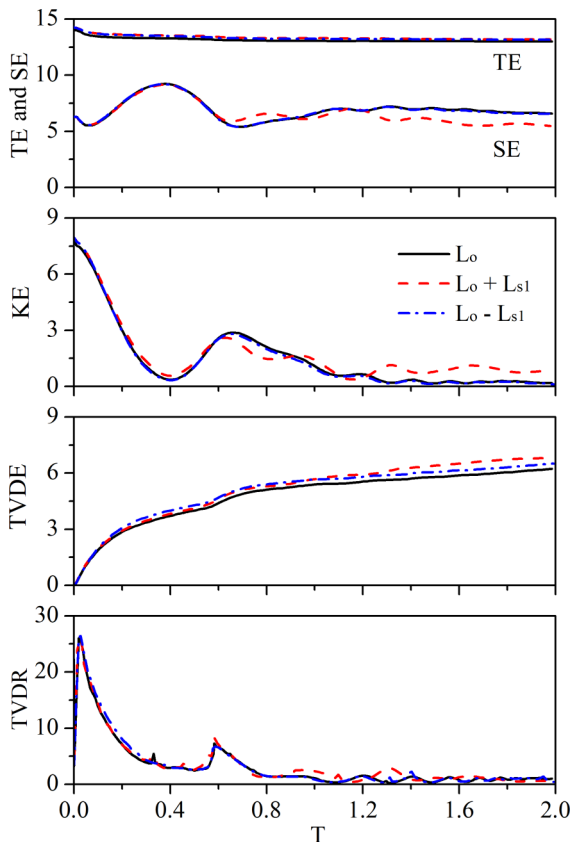
FIG. 10. Energy budget of the cases for the nearly head-on collision at We $= 61.4$ and $B = 0.15$ that are extracted from Fig. 9, in which the total energy (TE), the surface energy (SE), the kinetic energy (KE), the total viscous dissipation energy (TVDE), and the total viscous dissipation rate (TVDR) are all nondimensional.

flow that suppresses the stretching separation, and consequently the ligament pinch-off occurs only on one side and no satellite droplet is formed. For the case shown in Fig. 13(b), the local stretching flows of two spinning droplets are both enhanced so the stretching separation readily occurs with a longer ligament, while for the case shown in Fig. 13(c), the local stretching flows of two droplets are both reduced so that no separation occurs. All these observations consolidate the finding that the local stretching flow associated with the angular momentum plays important roles in promoting or suppressing the stretching separation for off-center collisions.

V. THEORETICAL MODEL FOR SPIN CHIRALITY EFFECTS ON DROPLET SEPARATION

A theoretical model for the criterion of reflexive and stretching separation based on the energy balance analysis for the collision between two nonspinning droplets is given in the Appendix. Here, we further propose an extended version of the model by accounting for the droplet spin chirality effects. It should be emphasized that the proposed model is used to qualitatively interpret the spinning effects on separation. A quantitatively predictive model requires comprehensive parametric study on all controlling parameters and indeed merits future study.

Apart from the inner reflexive and stretching flows induced by the off-center collision, the droplet spin motion induces an internal rotating flow with the velocity $U_{\mathrm{ro}} \sim R\omega_0$, which results in an additional viscous dissipation in stage II proportional to $\mu(U_{\mathrm{ro}}/R)^2(\frac{4}{3}\pi R^3)\sqrt{\rho_l R^3/\sigma}/8\pi R^2\sigma$, and
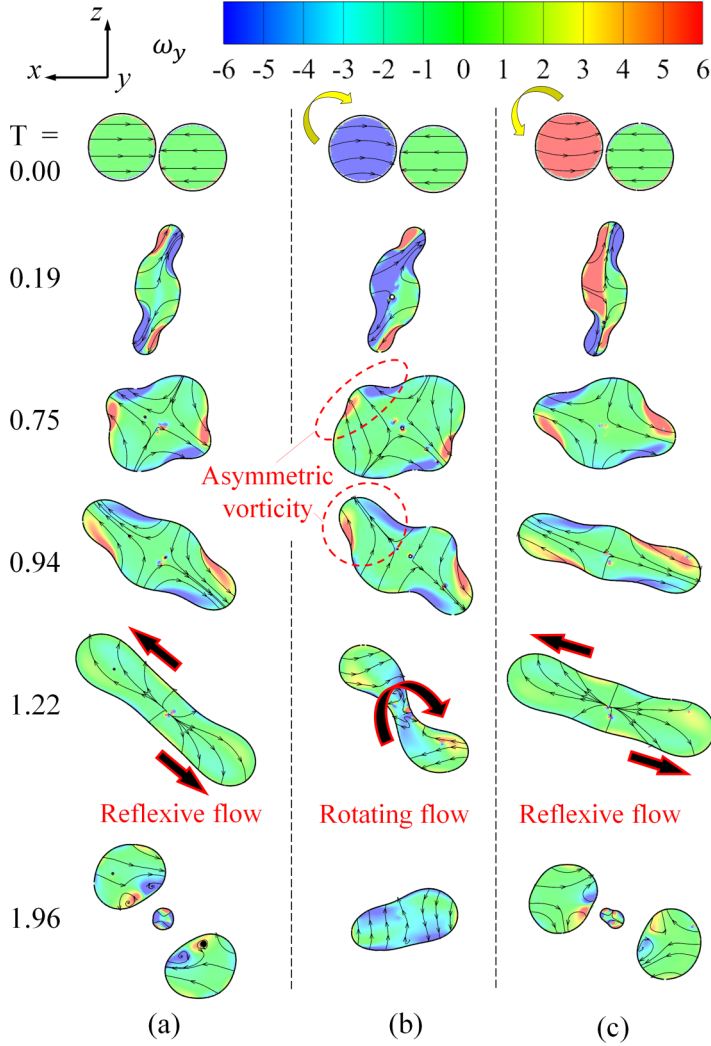
FIG. 11. Contour of the vorticity field and streamlines for droplet reflexive separation that are shown in Fig. 10 for the case of (a) two nonspinning droplets and the cases of one spinning droplet with (b) $\boldsymbol{\omega}_0\hat{y} = -3$ and (c) $\boldsymbol{\omega}_0\hat{y} = 3$.

its nondimensional form is given by

$$\Phi_{\mathrm{II,ro}} = \beta_5 \mathrm{OhWe}_{\mathrm{s}}, \tag{9}$$

where $\mathrm{We}_{\mathrm{s}} = \rho_l D_l (R\omega_0)^2/\sigma$ is the defined spin Weber number. The total viscous dissipation during stage II is given by $\Phi_{\mathrm{II}} = \Phi_{\mathrm{II,r}} + \Phi_{\mathrm{II,s}} + \Phi_{\mathrm{II,ro}}$, which degenerates to (A3) for the nonspinning cases. Regarding the energy balance analysis, the droplet spin motion affects the additional rotational kinetic energy (RKE$_0$) given by

$$\mathrm{RKE}_0 = \frac{\boldsymbol{L}_{\mathrm{s1}}^2}{2I_{y1}} = \frac{\mathrm{We}_{\mathrm{s}}}{60}, \tag{10}$$

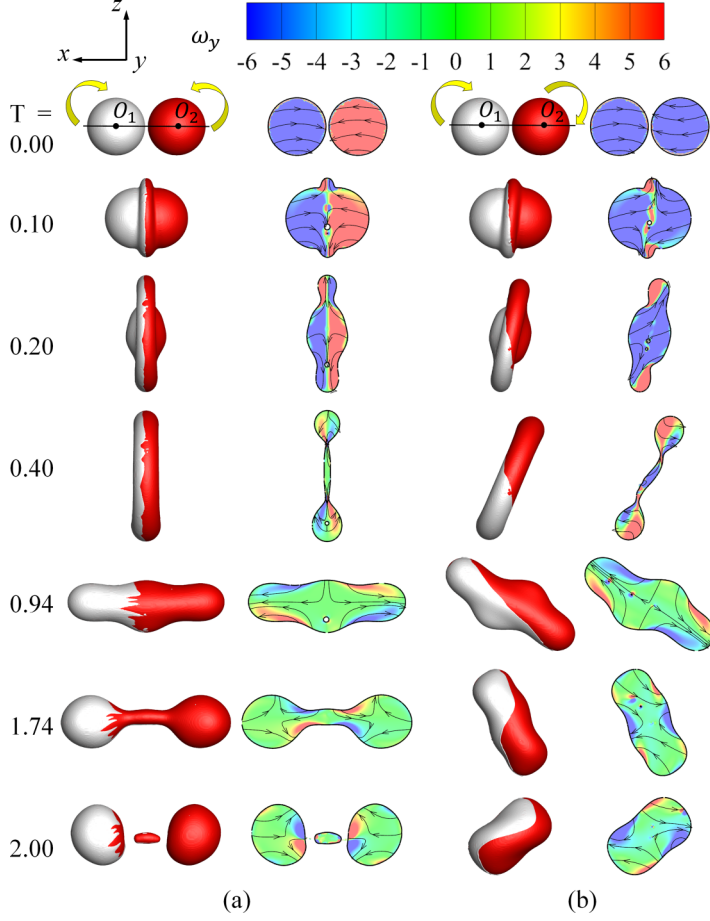where $\boldsymbol{L}_{\mathrm{s1}}$ is the spin angular momentum given by Eq. (7a).

FIG. 12. Droplet deformation and vorticity contour for a head-on collision between two spinning droplets at We = 61.4, Oh = 0.028, and $\omega_0 = 3$. The spin motions have the (a) opposite direction and (b) the same direction.

The droplet spin motion influences the local stretching flow. As we have seen in Fig. 7, due to the asymmetric kinetic energy distribution during the droplet rotation and separation stage, the ligament length can be either enhanced or reduced on the side with the mass liquid connected to the spinning droplet by increasing or decreasing the total angular momentum, respectively. Thus, the local stretching flow $U_{\text{s,eff}}$ influenced by the droplet spin motion must be modified as $U_{\text{s,eff}} \sim U_{\text{s}} + \beta_6 \eta R \omega_0$, where $\eta = (\boldsymbol{L_\text{o}} \cdot \boldsymbol{L_\text{s1}})/|\boldsymbol{L_\text{o}} \cdot \boldsymbol{L_\text{s1}}| = 1$ (or -1) corresponding to $\boldsymbol{L_\text{o}}$ and $\boldsymbol{L_\text{s1}}$ having the same (or opposite) direction.

Following the derivations expatiated in the Appendix, we can obtain the modified moment of inertia and effective rotational kinetic energy ($E_{\text{r,eff}}$) of the merged droplet by replacing the stretching velocity U_{s} with the effective local stretching velocity $U_{\text{s,eff}}$. Consequently, Eq. (A7) can be modified as

$$(1 - \alpha)\text{We} + \alpha \text{We} B^2 > \beta_1 \text{Oh}(1 + \beta_2/\beta_1 \sqrt{\text{We} B^2} + \beta_5/\beta_1 \text{We}_\text{s})$$

$$+ \gamma + \frac{\beta_4 \text{We}_\text{eff} B^2}{(\beta_3 \text{We}_\text{eff} B^2)^{-2} + (\beta_3 \text{We}_\text{eff} B^2)^2} - \frac{\text{We}_\text{s}}{60}, \tag{11}$$
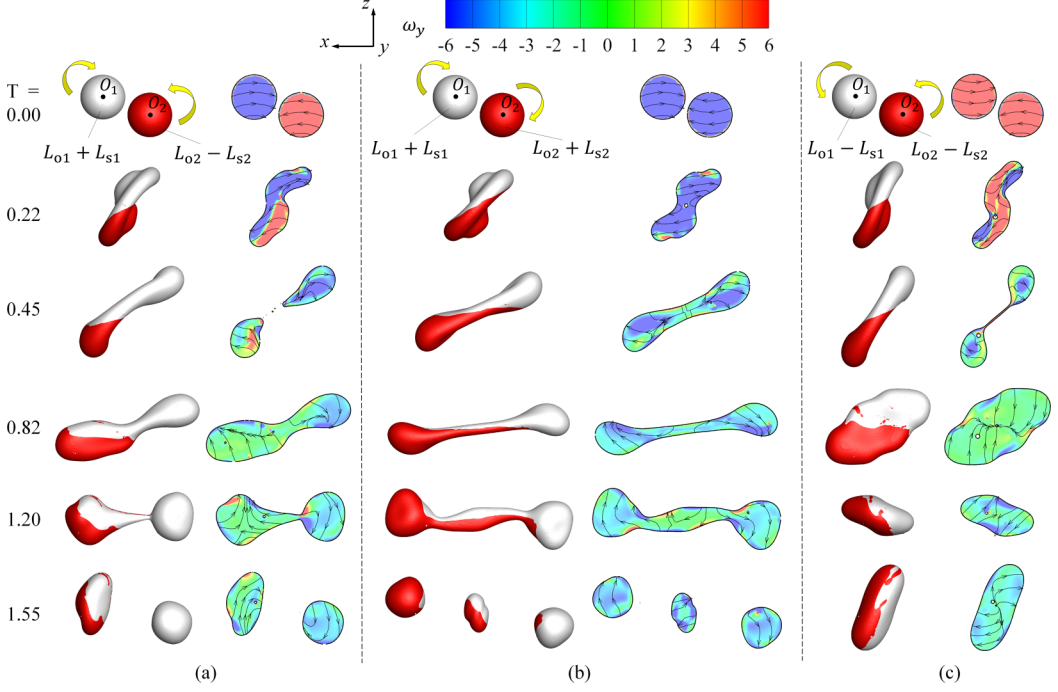
FIG. 13. Droplet deformation and vorticity contour for an off-center collision between two spinning droplets at We = 61.4, Oh = 2.8×10^{-2}, $B = 0.4$, and $\omega_0 = 3$. The spin motions have (a) opposite direction (droplet spin of O_1 is clockwise), (b) the same direction but droplet spin of O_1 is clockwise, and (c) the same direction but droplet spin of O_1 is anticlockwise.

where $\mathrm{We_{eff}}B^2 = (\sqrt{\mathrm{We}B^2} + \beta_6\eta\sqrt{\mathrm{We_s}})^2$ is the effective tangential component of stretching inertia. By using the same fitting coefficients given in the Appendix ($\alpha = 0.5$, $\beta_1 = 30$, $\gamma = 15$, $\beta_2 = 30$, $\beta_3 = 0.3$, and $\beta_4 = 20$) for the collisions between two nonspinning droplets, Fig. 14 compares the predicted boundaries with different values of β_5 and β_6. It is seen that the predicted boundaries are not sensitive to the variation of β_5 and β_6 in wide ranges, and $\beta_5 = 3$ and $\beta_6 = 0.1$ produce the best fitting to the present computational results. As shown in Figs. 14(a) and 14(c), by increasing β_5, the boundary shifts towards a larger $\mathrm{We}(1 - B^2)$ owing to the increased viscous dissipation induced by the droplet spin motion. By increasing β_6, the boundary shifts towards a smaller $\mathrm{We}B^2$ as shown in Fig. 14(b) because the reflexive separation is suppressed while the stretching separation is promoted by the positive spin (with $\eta = 1$) as seen in Fig. 9(b); conversely the boundary shifts towards a larger $\mathrm{We}B^2$ as shown in Fig. 14(d) because of the negative spin (with $\eta = -1$) as seen in Fig. 9(c).

Figure 15 further compares the predicted boundaries for three representative cases shown in Fig. 9. With increasing L_t, the lower branch of a boundary shifts towards a larger $\mathrm{We}(1 - B^2)$, while the upper branch shifts towards a smaller $\mathrm{We}B^2$. This indicates that the present theoretical model can qualitatively predict the chirality of spinning effects on the coalescence-separation transition where increasing the total angular momentum suppresses the reflexive separation but promotes the stretching separation.

VI. CONCLUSIONS

A computational study on droplet separation that is influenced by the droplet spin motion was investigated based on a validated volume-of-fluid method. The results show that droplet spin motion influences the reflexive and stretching separation in different ways. For the nearly head-on collisions,
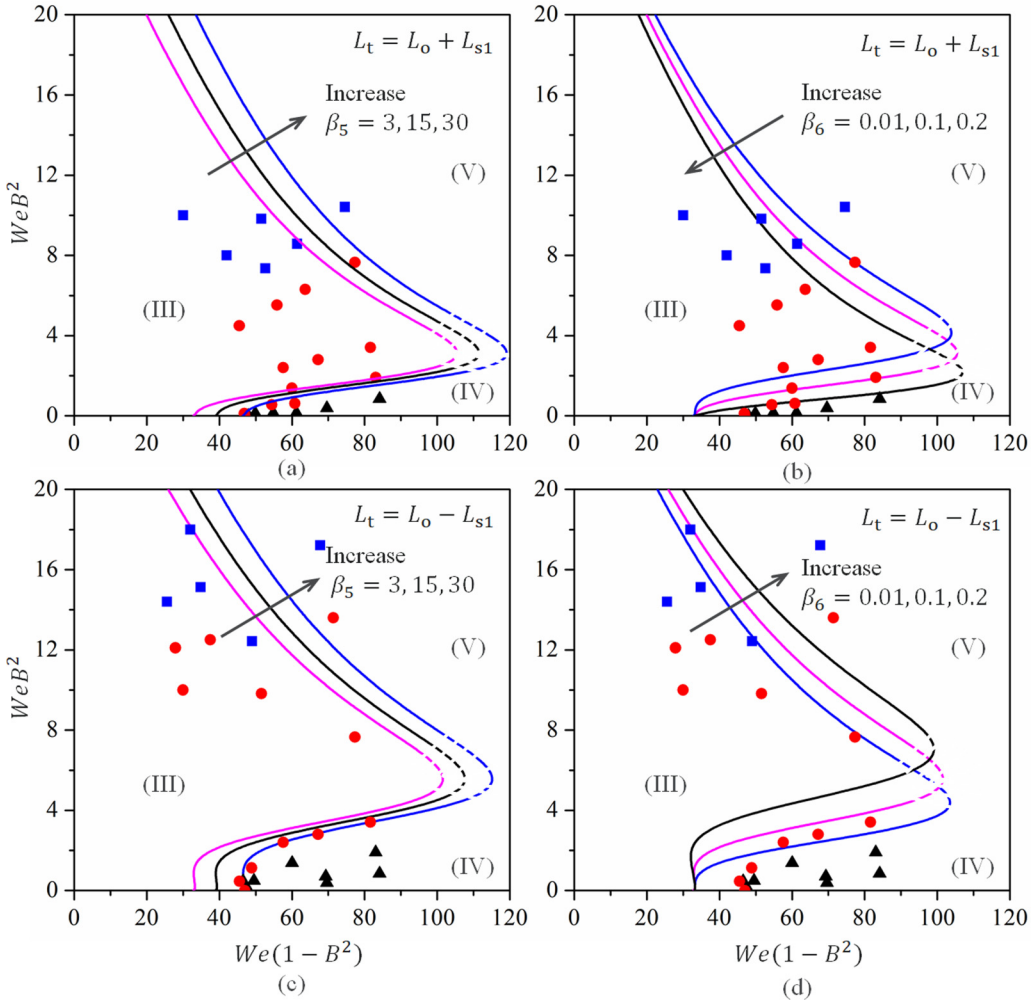
FIG. 14. Comparison of the predicted boundary for separations upon the collision between a spinning and a nonspinning droplet in Fig. 9. For sensitivity analysis, different values of β_5 and β_6 in large ranges are shown as (a) β_5 and (b) β_6 for $L_t = L_o + L_{s1}$; (c) β_5 and (d) β_6 for $L_t = L_o - L_{s1}$.

as the spin angular momentum of the spinning droplet is increased, the reflexive separation tends to be suppressed owing to the enhanced viscous dissipation and the induced inner rotating flow that diminishes the reflexive flow. For the collisions at larger impact parameters, the stretching separation is promoted by the local enhanced stretching flow. For the nearly grazing collisions, a longer ligament is formed and breaks into more satellite droplets, in which the liquid mass from the initial spinning droplet can reserve partial spin angular momentum.

The key physics underlying the rich phenomena is that the interplay between the initial spin angular momentum of a spinning droplet and the orbital angular momentum. This can be further illustrated by changing the chirality of droplet spin, which results in an augmented or reduced total angular momentum. For the nearly head-on collisions, it is found that the inner rotating flow is a decisive factor accounting for the influence of the spin chirality on the reflexive separation. For the collisions at larger impact parameters, the stretching separation depends on the local stretching flow, which is enhanced or reduced by the increase or decrease of total angular momentum.
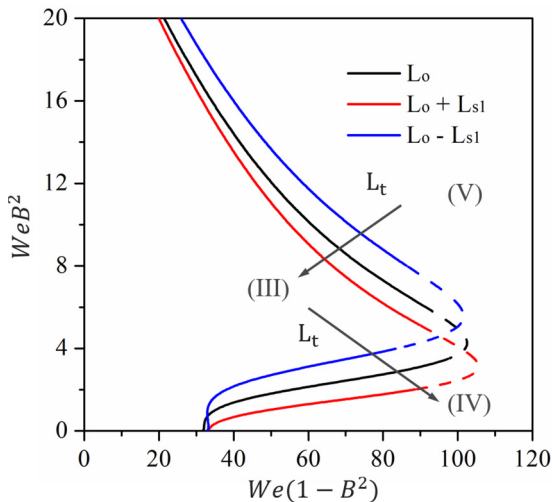
FIG. 15. Comparison of the predicted boundaries of three representative cases in Fig. 9, (a) two nonspinning droplets, (b) $\boldsymbol{\omega}_0 \hat{y} = -3$, and (c) $\boldsymbol{\omega}_0 \hat{y} = 3$.

A theoretical model for the reflexive and stretching separation from the aspect of energy balance analysis is proposed for the collisions involving spinning droplets. It can qualitatively reflect the nonmonotonicity of the separation varying with the impact parameter from reflexive separation to coalescence and to stretching separation. The key component of the model responsible for the nonmonotonicity is the rotational kinetic energy, which plays an important role in affecting the droplet separation but was not considered in previous modeling studies. By taking into account the contribution of droplet spin in the rotational kinetic energy, the model can also qualitatively explain the effects of droplet spin chirality on suppressing the reflexive separation while promoting the stretching separation by increasing the total angular momentum.

The present work shows that the rotational kinetic energy of the merged droplet can be a suppressing factor to the droplet separation instead of a promoting factor. This is because for the collision system of two droplets, the total angular momentum is conserved whereas the rotational kinetic energy varies with the moment of inertia due to the evolution of droplet deformation, and thereby the increase of rotational kinetic energy tends to reduce the reflexive or stretching kinetic energy (accounts for the reflexive and stretching separation, respectively) and leads to the droplet coalescence.

The off-center collision between spinning droplets with arbitrary polar and azimuthal angles of their spin axes is an apparent and necessary extension of the present work, but such future work would certainly be more complex than the present work due to breaking more symmetries that help simplify the present problem. Additionally, the experimental confirmation of the present computational results is of significance but is challenging, because it may require some innovations of the current experimental techniques in generating and visualizing spinning droplets.
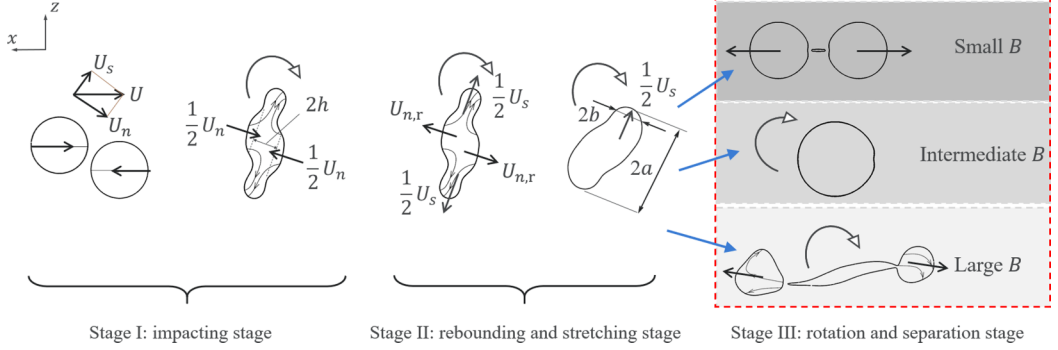
FIG. 16. Schematic of the model adopted in analyzing droplet reflexive and stretching separation for the collision between two nonspinning droplets.

APPENDIX: THEORETICAL MODEL FOR UNIFIED SEPARATION OF NONSPINNING DROPLETS

In previous studies on nonspinning droplet collision [4,5], energy balance analysis was applied to model reflexive separation and stretching separation of two nonspinning droplets, respectively. In this Appendix, a unified model will be proposed for droplet separation of two nonspinning droplets at arbitrary B. As shown in Fig. 16, the entire collision process is divided into three distinct stages: (I) the impacting stage from the instant upon droplet collision to that when the normal component of impact inertia (associated with the normal component of impact velocity, $U_n = U\sqrt{1 - B^2}$) has been completely converted into surface energy and viscous dissipation; (II) the rebounding stage (owing to the surface energy converted into reflexive inertia) for reflexive separation and the stretching stage (continuing stretching owing to the tangential component of impacting inertia that is associated with the tangential component of impact velocity $U_s = UB$) for stretching separation, respectively; and (III) the rotation and separation stage for the rotating droplet (owing to the nonzero angular momentum of the collision system), which appears different outcomes with varying B.

In stage I, the characteristic time can be estimated to be on the order of $2R/U_n$; the order of magnitude of the strain rate in the stagnation flow region is U_n/h, where the characteristic width $h \sim 2\mu_l/\rho_l U_n$ is obtained by using the stress balance relation $\frac{1}{2}\rho_l U_n^2 \sim \mu_l U_n/h$; the volume of the stagnation flow region is of the order of $(2h)(\pi R^2)$. Thus, most of the viscous dissipation in stage I is due to the viscous dissipation in the stagnation flow region, proportional to $[\mu_l (U_n/h)^2 (2\pi h R^2)(2R/U_n)]/8\pi R^2 \sigma$, and its nondimensional form is given by

$$\Phi_{\mathrm{I}} = \alpha \mathrm{We}(1 - B^2), \tag{A1}$$

where $0 < \alpha < 1$ is a proportionality factor to be determined by fitting experiments. Jiang *et al.* [4] found that $\alpha = 0.5$ is a universal coefficient for the cases of $B = 0$.

In stage II of the rebounding or stretching stage, the viscous dissipation is caused by both the reflexive flow and the stretching flow. The reflexive flow is driven by the surface tension and satisfies the relation of $\frac{1}{2}\rho_l U_{n,r}^2 \sim \sigma/R$, and the stretching flow is approximately estimated by $U_s = UB$. The characteristic time for reflexive separation is estimated to be the order of the natural oscillation time $t = \sqrt{\rho_l R^3/\sigma}$, whereas that for stretching separation is of the order of $2R/U_s$. Thereby, the viscous dissipation due to the reflexive flow is proportional to $\mu_l (U_{n,r}/R)^2 (\frac{4}{3}\pi R^3)\sqrt{\rho_l R^3/\sigma}/8\pi R^2 \sigma$, and its nondimensional form is given by

$$\Phi_{\mathrm{II,\,r}} = \beta_1 \mathrm{Oh}, \tag{A2a}$$

and the viscous dissipation due to the stretching flow is proportional to $\mu_l(U_s/R)^2(\frac{4}{3}\pi R^3)(2R/U_s)/8\pi R^2\sigma$, and its nondimensional form is given by

$$\Phi_{\text{II,s}} = \beta_2 \text{Oh}\sqrt{\text{We}B^2}. \tag{A2b}$$

The total viscous dissipation during stage II is approximated by

$$\Phi_{\text{II}} = \Phi_{\text{II,r}} + \Phi_{\text{II,s}}. \tag{A3}$$

Qian and Law [5] suggested $\beta_1 = 30$ by fitting their experimental data for head-on collisions.

In stage III of the rotating and separation stage, the off-center collision-induced rotation motion suppresses the droplet separation, owing to the conversion of initial orbital angular momentum $\boldsymbol{L}_o$ into the spin angular momentum $\boldsymbol{L}_s$ of the merged droplet. As shown in Fig. 16, the critical droplet deformation at small B is approximately two spheres connected by a short ligament, that at intermediate B is approximately a larger sphere, and that at large B is approximately two spheres connected by a long ligament. The characteristic length of the round head of the stretching ligament is $2b$, as shown in Fig. 16, which can be estimated by the balance between the surface tension pressure and the stagnation pressure as $\sigma/b \sim \frac{1}{2}\rho_l U_s^2$, yielding $b \sim 2\sigma/\rho_l U_s^2$ and $a \sim R^2/b$ by the volume conservation.

The moment of inertia of the merged droplet (or approximating a stretching ligament) based on the spinning axis (y axis) is estimated by

$$I_y = \frac{1}{5}m(a^2 + b^2) \sim \rho_l R^5\left[\frac{1}{(\beta_3 \text{We}B^2)^2} + (\beta_3 \text{We}B^2)^2\right]. \tag{A4}$$

The proportionality factor β_3 appears symmetrically in (A4) for mathematical convenience. Physically, I_y varies nonmonotonically with $\text{We}B^2$ and reaches its minimum value at $\text{We}B^2 \sim 1/\beta_3$. For nonspinning droplet collision, $\boldsymbol{L}_t = \boldsymbol{L}_o$ is given in Eq. (7). Consequently, the rotational kinetic energy ($E_r = \boldsymbol{L}_t^2/2I_y$) of the merged droplet, normalized by $8\pi R^2\sigma$, can be given by

$$E_r = \frac{\beta_4 \text{We}B^2}{(\beta_3 \text{We}B^2)^{-2} + (\beta_3 \text{We}B^2)^2}. \tag{A5}$$

The physical criterion from the perspective of energy balance is that the separation occurs if the viscous dissipation (in stages I and II) and E_r in stage III are smaller than the excessive kinetic energy so that the merged droplet cannot hold. This criterion can be expressed in a nondimensional form as

$$E_{k0} + E_{s0} > \Phi_{\text{I}} + \Phi_{\text{II}} + E_r + E_s, \tag{A6}$$

in which E_{k0} is the nondimensional initial impacting kinetic energy, E_{s0} the initial surface energy, and E_s the surface energy of the merged droplet at the instant when they are about to separate. Following Qian and Law [5], we defined the surface energy addition $\gamma = E_s - E_{s0}$, where $\gamma = 15$ for head-on collisions.

Consequently, by substituting Eqs. (A1), (A3), and (A5) into Eq. (A6), we obtain the transition boundary for separation as

$$(1-\alpha)\text{We} + \alpha\text{We}B^2 > \beta_1\text{Oh}(1 + \beta_2/\beta_1\sqrt{\text{We}B^2}) + \gamma + \frac{\beta_4\text{We}B^2}{(\beta_3\text{We}B^2)^{-2} + (\beta_3\text{We}B^2)^2}. \tag{A7}$$

For head-on collisions ($B = 0$), Eq. (A7) can be degenerated into

$$(1-\alpha)\text{We}_c > \beta_1\text{Oh} + \gamma, \tag{A8}$$

which is exactly the same as the equation derived by Qian and Law [5].

To determine proportionality factors, we applied the previous results and scaling analysis. Specifically, $\alpha = 0.5$ is consistent with previous results in [4,5]; $\beta_1 = 30$ and $\gamma = 15$ were suggested
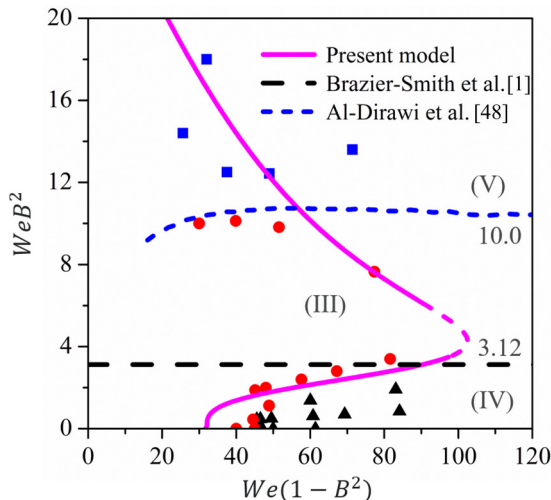
FIG. 17. Predicted boundary for the reflexive and stretching separation of two nonspinning droplets in the parameter space $We(1 - B^2) \sim WeB^2$. The dashed curve indicates the occurrence of droplet coalescence, which cannot be predicted by the present model. The criteria of Brazier-Smith *et al.* [1] and Al-Dirawi *et al.* [48] are also plotted for comparison.

by Qian and Law [5] by a fitting experiment for the head-on collision; $\beta_3 = 0.3$ is consistent with the estimate of $\beta_3 \sim (WeB^2)^{-1} \sim O(10^{-1})$ for droplet collisions in the parameter range of $We \sim O(10^2)$ and $B^2 \sim O(10^{-1})$; and $\beta_4 = 20$ accords with $\beta_4 \sim O(10)$, which follows from the relation $\beta_4 WeB^2 \sim We$ because the initial impact kinetic energy (E_{k0}) and E_r have the same order of magnitude.

The predicted boundary for reflexive and stretching separations by using (A7) with the above factors is shown in Fig. 17. It is seen that (A7) can qualitatively reflect the trends of reflexive separation and stretching separation with varying B and We. It is noted that a part of the predicted boundary around a turning point is shown by a dashed curve because droplet coalescence actually occurs. It is a common phenomenon in many physics problems [46,47] that a turning point separates the boundary to two stable branches (here, the lower branch is for reflexive separation and the upper branch for stretching separation), and that the unstable nature of the problem around the turning point often requires additional physics. The present model cannot predict the occurrence of droplet coalescence because it does not account for a few key physics, such as gas film drainage, rarefied gas effects, and van der Waals force. A unified model that is able to predict both separation and coalescence certainly merits future studies.

In the model of Brazier-Smith *et al.* [1], the rotational energy was calculated at the initial time instant, and its variation with the evolution of droplet deformation was neglected. In the model of Al-Dirawi *et al.* [48], the boundary between coalescence and stretching separation is nearly uninfluenced by varying droplet viscosity in a wide range. We compared the results predicted by the model of Brazier-Smith *et al.*, the model of Al-Dirawi *et al.*, and our model, as shown in Fig. 17. The model of Brazier-Smith *et al.* predicts a line boundary of $WeB^2 = 3.12$, and that of Al-Dirawi *et al.* predicts an approximate line boundary of $WeB^2 = 10.0$. Both models indicate that the tangential component of impacting inertia, WeB^2, plays a dominant role in affecting droplet separation, but our model takes into account the normal component of impacting inertia, $We(1 - B^2)$, and predicts that the boundary nonmonotonically varies with WeB^2.

To examine the sensitivity of the prediction by (A7) to the proportionality factors, particularly β_2, β_3, and β_4, we further compare the predicted boundaries by using different values of β_2, β_3, and β_4, as shown in Fig. 18. All the boundary curves show the same qualitative trend by varying the
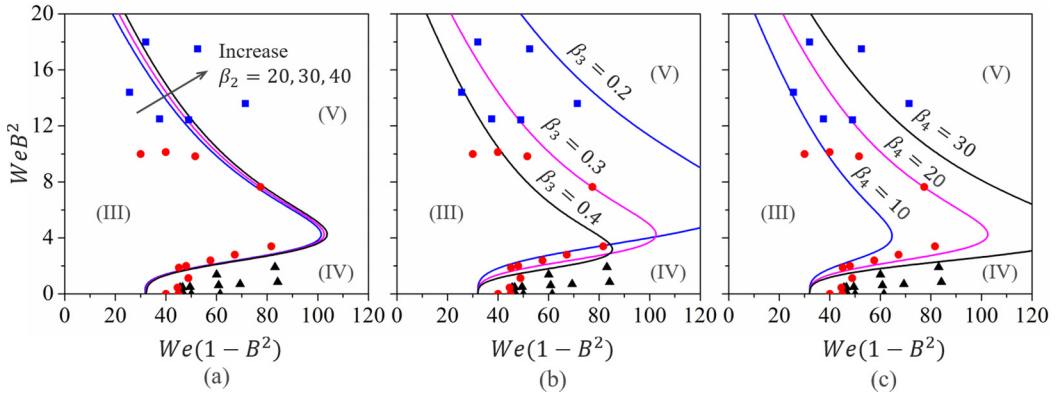
FIG. 18. Comparison of the predicted boundaries with different proportionality factors: (a) β_2, (b) β_3, and (c) β_4.

proportionality factors in a wide range, and these results validate the estimated orders of magnitude of these proportionality factors in the present model. Specifically, the boundary curves are slightly shifted towards a larger $We(1 - B^2)$ by increasing β_2 owing to the increased viscous dissipation. Decreasing β_3 or increasing β_4 tend to enhance the amount of rotational kinetic energy so droplet separation is suppressed with the enlarged regime of droplet coalescence (III). This indicates that the rotational kinetic energy plays an important role in affecting the droplet separation.

[1] P. R. Brazier-Smith, S. G. Jennings, and J. Latham, The interaction of falling water drops: Coalescence, Proc. R. Soc. London, Ser. A **326**, 393 (1972).

[2] S. G. Bradley and C. D. Stow, Collisions between liquid drops, Proc. R. Soc. A **287**, 635 (1978).

[3] N. Ashgriz and J. Y. Poo, Coalescence and separation in binary collisions of liquid drops, J. Fluid Mech. **221**, 183 (1990).

[4] Y. J. Jiang, A. Umemura, and C. K. Law, An experimental investigation on the collision behaviour of hydrocarbon droplets, J. Fluid Mech. **234**, 171 (1992).

[5] J. Qian and C. K. Law, Regimes of coalescence and separation in droplet collision, J. Fluid Mech. **331**, 59 (1997).

[6] J.-P. Estrade, H. Carentz, G. Lavergne, and Y. Biscos, Experimental investigation of dynamic binary collision of ethanol droplets–a model for droplet coalescence and bouncing, Int. J. Heat Fluid Flow **20**, 486 (1999).

[7] G. Brenn and V. Kolobaric, Satellite droplet formation by unstable binary drop collisions, Phys. Fluids **18**, 087101 (2006).

[8] C. Gotaas, P. Havelka, H. A. Jakobsen, H. F. Svendsen, M. Hase, N. Roth, and B. Weigand, Effect of viscosity on droplet-droplet collision outcome: Experimental study and numerical comparison, Phys. Fluids **19**, 102106 (2007).

[9] K.-L. Pan, P.-C. Chou, and Y.-J. Tseng, Binary droplet collision at high Weber number, Phys. Rev. E **80**, 036301 (2009).

[10] C. Rabe, J. Malet, and F. Feuillebois, Experimental investigation of water droplet binary collisions and description of outcomes with a symmetric Weber number, Phys. Fluids **22**, 047101 (2010).

[11] C. Tang, P. Zhang, and C. K. Law, Bouncing, coalescence, and separation in head-on collision of unequal-size droplets, Phys. Fluids **24**, 022101 (2012).

[12] M. Sommerfeld and M. Kuschel, Modelling droplet collision outcomes for different substances and viscosities, Exp. Fluids **57**, 187 (2016).

[13] G. Finotello, R. F. Kooiman, J. T. Padding, K. A. Buist, A. Jongsma, F. Innings, and J. Kuipers, The dynamics of milk droplet–droplet collisions, Exp. Fluids **59**, 17 (2018).

[14] K. H. Al-Dirawi and A. E. Bayly, A new model for the bouncing regime boundary in binary droplet collisions, Phys. Fluids **31**, 027105 (2019).

[15] G. Brenn, Droplet collision, in *Handbook of Atomization and Sprays*, edited by N. Ashgriz (Springer, Berlin, 2011), p. 157–181.

[16] M. Orme, Experiments on droplet collisions, bounce, coalescence and disruption, Prog. Energy Combust. Sci. **23**, 65 (1997).

[17] N. Roth, C. Rabe, B. Weigand, F. Feuillebois, and J. Malet, Droplet collision outcomes at high Weber number, in *Proceedings of the 21st Conference on Liquid Atomization and Spray Systems* (ILASS, Mugla, Turkey, 2007).

[18] L. Reitter, M. Liu, J. Breitenbach, K.-L. Huang, D. Bothe, G. Brenn, K.-L. Pan, I. Roisman, and C. Tropea, Experimental and computational investigation of binary drop collisions under elevated pressure, in *Proceedings of ILASS Europe. 28th European Conference on Liquid Atomization and Spray Systems* (ILASS, Valencia, Spain, 2017).

[19] K. Krishnan and E. Loth, Effects of gas and droplet characteristics on drop-drop collision outcome regimes, Int. J. Multiphase Flow **77**, 171 (2015).

[20] F. Blanchette, L. Messio, and J. W. M. Bush, The influence of surface tension gradients on drop coalescence, Phys. Fluids **21**, 072107 (2009).

[21] K. Sun, P. Zhang, Z. Che, and T. Wang, Marangoni-flow-induced partial coalescence of a droplet on a liquid/air interface, Phys. Rev. Fluids **3**, 023602 (2018).

[22] F. Jia, K. Sun, P. Zhang, C. Yin, and T. Wang, Marangoni effect on the impact of droplets onto a liquid-gas interface, Phys. Rev. Fluids **5**, 073605 (2020).

[23] K. Sun, F. Jia, P. Zhang, L. Shu, and T. Wang, Marangoni Effect in Bipropellant Droplet Mixing during Hypergolic Ignition, Phys. Rev. Appl. **15**, 034076 (2021).

[24] G. Finotello, J. T. Padding, N. G. Deen, A. Jongsma, F. Innings, and J. Kuipers, Effect of viscosity on droplet-droplet collisional interaction, Phys. Fluids **29**, 067102 (2017).

[25] A. Moreira, A. Moita, and M. Panao, Advances and challenges in explaining fuel spray impingement: How much of single droplet impact research is useful?, Prog. Energy Combust. Sci. **36**, 554 (2010).

[26] R. Kamali and M. Mofarrahi, Numerical investigation of various spray breakup and droplet collision models in the modeling of in-cylinder fuel spray, Atomization Sprays **22**, 843 (2012).

[27] M. Sommerfeld and L. Pasternak, Advances in modelling of binary droplet collision outcomes in sprays: A review of available knowledge, Int. J. Multiphase Flow **117**, 182 (2019).

[28] K.-L. Pan, K.-L. Huang, W.-T. Hsieh, and C.-R. Lu, Rotational separation after temporary coalescence in binary droplet collisions, Phys. Rev. Fluids **4**, 123602 (2019).

[29] X. Chen and V. Yang, Thickness-based adaptive mesh refinement methods for multi-phase flow simulations with thin regions, J. Comput. Phys. **269**, 22 (2014).

[30] C. He, X. Xia, and P. Zhang, Non-monotonic viscous dissipation of bouncing droplets undergoing off-center collision, Phys. Fluids **31**, 052004 (2019).

[31] C. He, X. Xia, and P. Zhang, Vortex-dynamical implications of nonmonotonic viscous dissipation of off-center droplet bouncing, Phys. Fluids **32**, 032004 (2020).

[32] C. He and P. Zhang, Nonaxisymmetric flow characteristics in head-on collision of spinning droplets, Phys. Rev. Fluids **5**, 113601 (2020).

[33] S. Popinet, An accurate adaptive solver for surface-tension-driven interfacial flows, J. Comput. Phys. **228**, 5838 (2009).

[34] S. Popinet, Numerical models of surface tension, Annu. Rev. Fluid Mech. **50**, 49 (2018).

[35] X. Chen, D. Ma, and V. Yang, Collision outcome and mass transfer of unequal-sized droplet collision, in *Proceedings of the 50th AIAA Aerospace Sciences Meeting* (AIAA, Reston, VA, 2012).

[36] X. Chen, D. Ma, V. Yang, and S. Popinet, High-fidelity simulations of impinging jet atomization, Atomization Sprays **23**, 1079 (2013).

[37] C. Hu, S. Xia, C. Li, and G. Wu, Three-dimensional numerical investigation and modeling of binary alumina droplet collisions, Int. J. Heat Mass Transfer **113**, 569 (2017).

[38] C. Tang, J. Zhao, P. Zhang, C. K. Law, and Z. Huang, Dynamics of internal jets in the merging of two droplets of unequal sizes, J. Fluid Mech. **795**, 671 (2016).

[39] X. Xia, C. He, D. Yu, J. Zhao, and P. Zhang, Vortex-ring-induced internal mixing upon the coalescence of initially stationary droplets, Phys. Rev. Fluids **2**, 113607 (2017).

[40] X. Xia, C. He, and P. Zhang, Universality in the viscous-to-inertial coalescence of liquid droplets, Proc. Natl Acad. Sci. USA **116**, 23467 (2019).

[41] P. Zhang and C. K. Law, An analysis of head-on droplet collision with large deformation in gaseous medium, Phys. Fluids **23**, 042102 (2011).

[42] X. Chen, D. Ma, P. Khare, and V. Yang, Energy and mass transfer during binary droplet collision, in *Proceedings of the 49th AIAA Aerospace Sciences Meeting* (AIAA, Reston, VA, 2011).

[43] S. Tanguy and A. Berlemont, Application of a level set method for simulation of droplet collisions, Int. J. Multiphase Flow **31**, 1015 (2005).

[44] K. Sun, P. Zhang, M. Jia, and T. Wang, Collision-induced jet-like mixing for droplets of unequal-sizes, Int. J. Heat Mass Transfer **120**, 218 (2018).

[45] C. He, L. Yue, and P. Zhang, A computational model for spinning effects on post-collision velocities of bouncing droplets, Atomization Sprays **31**, 43 (2021).

[46] F. A. Williams, *Combustion Theory*, 2nd ed. (CRC Press, Boca Raton, FL, 2018).

[47] V. I. Arnol'd, *Catastrophe Theory* (Springer Science & Business Media, Berlin, 2003).

[48] K. H. Al-Dirawi, K. H. Al-Ghaithi, T. C. Sykes, J. R. Castrejón-Pita, and A. E. Bayly, Inertial stretching separation in binary droplet collisions, J. Fluid Mech. **927**, A9 (2021).